# Minimizing Sheet Resistance of Organic Photovoltaic Cell Top Contact Electrode Layer: Silver Nanowire Concentration vs. Conductive Polymer Doping Concentration

Caitlyn Cook

*June 2015*
*Materials Engineering Department,*
*California Polytechnic State University-San Luis Obispo*
*Dr. Linda Vanasupa | Next Energy Technology Inc.*

**Table of Contents:**

## I. Abstract

The top contact electrode layers of nine organic photovoltaic cells were prepared with two varying factors: three Silver nanowire (AgNW) densities deposited on a conductive polymer doped with three concentrations. Silver's low sheet resistance of 20-Ω/sq is hypothesized to lower the sheet resistance of the anode layer and thus enhance the overall efficiency of the cell. Four-point probe measurements indicated that increasing AgNW density in the top contact electrode layer of an organic photovoltaic cell significantly reduces sheet resistance from 52.2k-Ω/sq to 18.0 Ω/sq. Although an increase in doping concentration of the conductive polymer reduced sheet resistance in low AgNW density samples from 52.2k-Ω/sq to 5.10k-Ω/sq, only a minor decrease from 34.7-Ω/sq to 29.2-Ω/sq was found in the higher AgNW density samples. To explain these patterns, we propose a transition in charge carrier conduction mechanism from one of resistors in series (AgNW and polymer matrix), controlled by the resistance of the conductive polymer, to that of a parallel circuit, with resistance controlled by the resistance of silver. Proposed models are supported by the number of disjoints between AgNWs found in Scanning Electron Microscope characterizations at 20,000X magnification. The number of disjointed AgNWs within 2.8 µm x 3.2-µm sections on the electrode surface decreased from an average of two to zero with increasing AgNW density. Atomic Force Microscopy characterizations portrayed increased RMS roughness due to AgNW agglomeration, ring shaped wire orientation and a random distribution of particles that potentially raise sheet resistance with increased contact resistance.

## II. Introduction

Organic Photovoltaic Cells (OPVC) have been a popular topic of research due to the low-cost processing and material costs, and high throughput production.[1] Two stacking architectures are commonly utilized during the fabrication of OPVCs (Figure 1). Studies have shown that inverse stacking structures have a longer lifetime and higher efficiencies due to the high work function metal at the top contact anode. OPVCs function by allowing photons from the sun to enter the cell through the transparent conducting oxide (TCO), which normally consists of a glass substrate with a metal oxide on top. The photon excites an electron, which produces an exciton. This exciton dissipates into holes and electrons once passing the bulk heterojunction (BHJ) interface due to the difference between the highest occupied molecular orbital levels of the donor and acceptor layers.[1] Each charge carrier utilizes its respective transport layer, either electron (ETL) or hole (HTL), in order to reach the cathode and anode, respectively. Charge accumulates at each electrode, inducing an electric field and thus generating current.

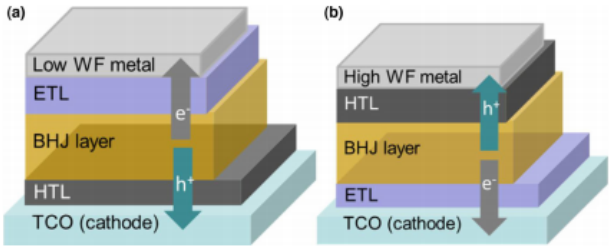


**Figure 1.** Illustration of a conventional (a) and an inverted (b) OPV cell stacking architecture.[1]

Current OPVC research is attempting to replace indium tin oxide (ITO) with AgNWs as the top contact electrode layer in inverted devices as prices for using indium raises and more flexible electronics are desired. According to David Cohen in 2007, indium's expected exhaustion time on earth was five to ten years, when compared to a 15 to 20 year exhaustion time for Silver.[2] ITO is the most commonly used transparent conductor in OPV cells due to its high transmittance (>90%) and low sheet resistance of 10-Ω/sq. on a glass substrate.[3] However, due to its slow vapor phase sputtering

processing methods, depositing indium onto a glass substrate can cost up to \$26 $m^{-2}$ for a 10-Ω/sq.[3] When compared to silver, the material cost of indium at \$600 $kg^{-1}$ is much less than silver's material cost at \$765 $kg^{-1}$, but since silver is deposited with a solution-phase coating process at a rate 100 times faster, its deposition cost is much less. Silver is also a suitable replacement due to its comparable transparent and conductive properties with 95% transparency at 20-Ω/sq.2

Due to the importance of the top electrode in determining the device efficiency of the OPVC as a whole, matching the performance of ITO is crucial. Implementing electrodes that are fully solution processed and that can be incorporated into the low-cost, high throughput processing are additional goals that researchers are trying to reach today. Using the solution-phase processing would increase manufacturing capital due to its efficiency in speed and ability to control nanowire dimensions to meet specified OPV cell performance. For example, depending on which solvent the nanowires are deposited in gauges dimensions of the diameter and length of the AgNWs.

In the polypol synthesis method of growing AgNWs in a dispersion prior to deposition, a reducing agent to convert silver ions into silver atoms and a capping agent to "direct the anisotropic assembly" of the silver atoms into nanowires are combined in a liquid solution.[4] Figure 2 displays a schematic of the growing process of a AgNWs. Heat was applied to the solution in order to reduce silver ions into atoms. These atoms

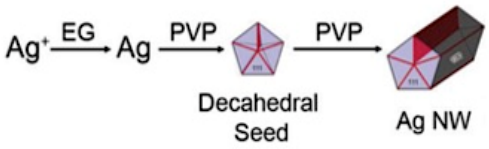


**Figure 2.** Conventional Polypol Synthesis of AgNWs.[4]

agglomerate to form nuclei until the energy to break the bonds in the nuclei exceeds the thermal energy present. Once this energy barrier has been reached and "freezes" in the multiply twinned decahedral morphology, a seed is produced. From this seed, silver atoms attach to the faces of the decahedra, leading to the elongation of nanorods (Figure 3), while the capping agent adheres to the sides of the nanorods to allow for anisotropic growth.[4]

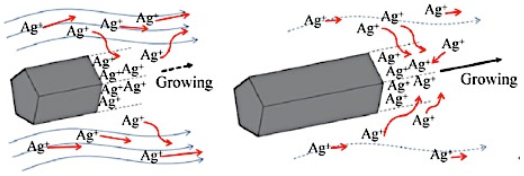


**Figure 3.** Pictorial representation of silver atoms agglomerating on the decahedral surface to form AgNWs.[3]

Controlling the reaction temperatures and stirring speeds during synthesis can modify dimensions of AgNWs. High aspect ratio AgNWs (wires with a much greater length than diameter) are formed by reducing reaction temperatures and increasing stirring speeds.[3] AgNWs with a high aspect ratio results in higher conductivities at low nanowire densities when maximizing the number of connections between nanowires[3]. By maximizing connections between nanowires, free charge carriers are able to select the most direct conducting path to traverse across, while taking the path with the least amount of contact junctions (Figure 4). Depending on the concentration of AgNWs deposited onto a substrate determines the amount of contact resistance that will be induced by the random overlapping of AgNWs (Figure 5). Where one AgNW overlaps another, a "contact junction" with contact resistance is formed. Growing longer nanowires enables a lower concentration of AgNWs to be deposited and results in less contact junctions. In the production of producing high aspect ratio AgNWs, sheet resistance from depositing standard AgNWs have been found to drop from $10^7$ Ω/sq. to 19Ω/sq.[3]

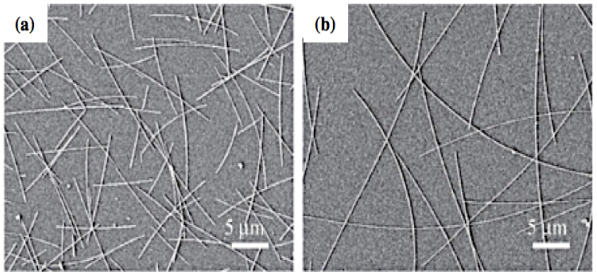


**Figure 4.** SEM images of (a) high concentration of AgNWs and (b) lower concentration of high aspect ratio AgNWs.[3]

Although high aspect ratio AgNWs are desired, electrical resistivity of the nanowire increases as the diameter becomes small relative to the mean free path of the free charge carrier.[4] Additionally, optical properties such as transparency and haze are

affected by the aspect ratio of AgNWs. On average, growing high aspect ratio AgNWs increases the optical transmission of the film while decreasing sheet resistance (Figure 5), but decreases the amount of haze. Haze is defined as the "percentage of transmitted light

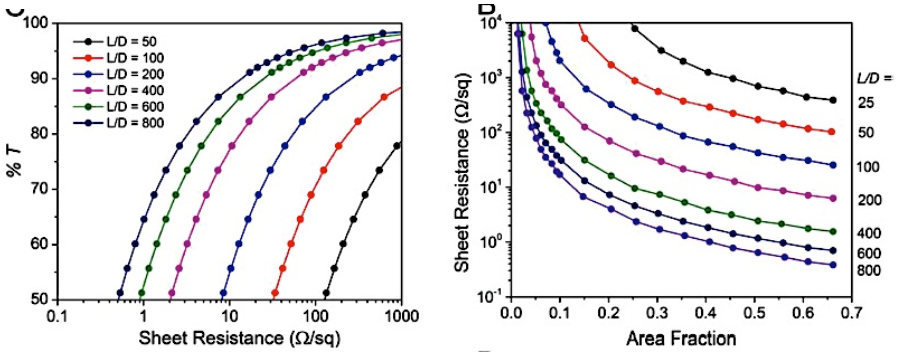


**Figure 5**. Left) Displaying how percent transmittance (%T) and sheet resistance is affected by aspect ratio (L/D). Right) The effect of aspect ratio and the number of nanowires per area (area fraction) on sheet resistance.[4]

which in passing through the film deviates more than 2.5 degrees from the incident beam by forward scattering".[4] An increase in the haze factor increases the efficiency of an OPVC due to the larger amount of scattered light emitted into the absorber material. However, producing a higher amount of forward scattered light requires a larger surface area, which implies that a larger AgNW diameter is needed. This illustrates the necessary distinction that has to be made in choosing the size of AgNWs that are to be implemented into the electrode film. If an OPVC is to have a stronger light absorption, the transmission will decrease along with increasing sheet resistance.

Depositing a conductive polymer down prior to the deposition of AgNWs can also reduce sheet resistance. Past studies have embedded AgNWs into the conductive polymer poly3,4-ethylenedioxythiophene:polystyrene-sulfonate (PEDOT:PSS) in an attempt to create organic-inorganic composite electrodes.[5] In doing so, wires sink into the conductive polymer, which flattens out the nanowires and reduces the overall surface roughness of the electrode. Additionally, as PEDOT:PSS fills in the gaps between AgNWs that failed to make contact, free charge carriers are able to flow across the polymer to continue their conducting paths. Figure 6 shows the organic structure of PEDOT:PSS which is fundamental in explaining how electrons are able to conduct through it. Due to the bond alternation of $\pi$ and $\sigma$ orbitals in the repeating benzene ring structures, delocalized valance and conduction wavefunctions form the alternating double

and single bonds, which support mobile charge carriers.[6] The unhybridized π bonding within the conjugated PEDOT:PSS structure allows electrons to "hop" across polymer chains when given energy from an externally applied electric field.

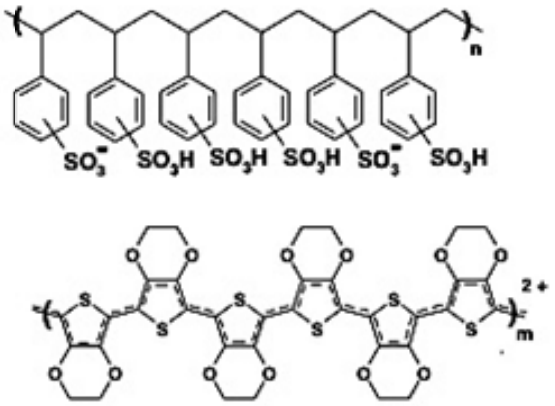


**Figure 6.** The molecular structure of PEDOT:PSS that displays the pi bonding that support conducting delocalized electrons.[7]

Doping a conductive polymer such as PEDOT with a polar solvent like PSS reduces sheet resistance with increasing PSS concentration. When adding a polar solvent additive into the PEDOT layer during spin coating, transformation of the resonant structure of PEDOT chains from the benzoid to the quinoid structure occur. This change enables initially coiled PEDOT chains to transform into a linear conformation, which allows for conjugated π-electrons to be delocalized over the entirety of the chain.[8] Delocalized π-electrons along linear chains enable more efficient charge-carrier mobility and thus decreases sheet resistance (Figure 7). However, conductivity of the polymer

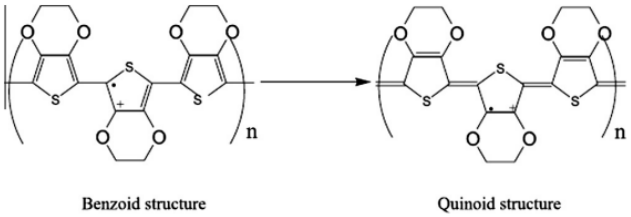


**Figure 7**. Linearizing PEDOT chains due to transformation of resonant structures.[9]

decreases when approaching a maximum doping concentration. This specific concentration maximum is dependent on the polar solvent utilized, but should be noted as a limit to the increase in conductivity. Studies have also reported that the reduction in sheet resistance is due to the surface roughness as resonant structures in polymer chains undergo transformation with increasing doping concentration (Figure 8).

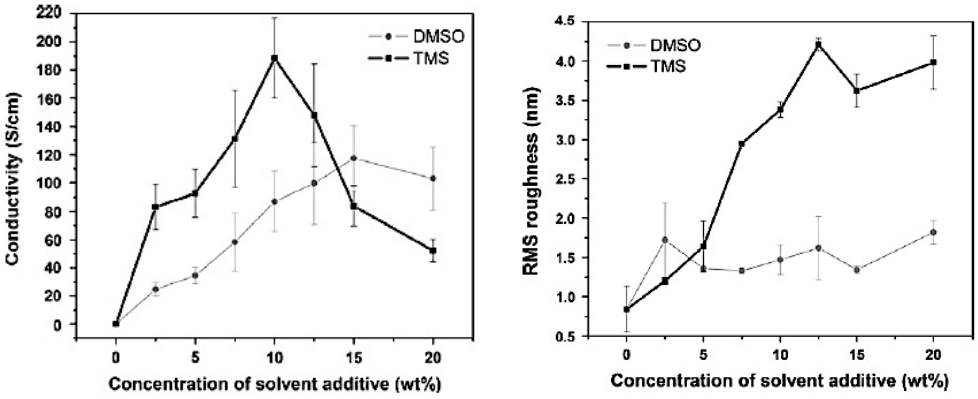


**Figure 8.** Left) Maximum doping concentrations of two polar solvents that result in a decrease in conductivity. Right) Increase in AFM root mean square (RMS) surface roughness with increasing doping concentration. [8]

As an increase in surface roughness of the conductive polymer poses as a benefit to sheet resistance results, deposition of a metal oxide on top of AgNWs in an inverted OPVC structure is also beneficial. Metal oxides deposited on top of AgNWs reduce charge carrier recombination rate and thus increase the efficiency of the cell as hole extraction is enhanced. Vacancies within the metal oxide layer due to oxygen deficiencies act as a bias as holes are drawn to the anode.[10]

## III. Materials and Methods

### III.I Film Synthesis

Nine OPVC samples were synthesized by NEXT Technologies and sent via mail for testing and characterization of the top contact electrode layer. All layers composing the cell samples were fabricated on top of a 15x15 mm glass substrate in the inverted stacking structure as displayed in Figure 9.

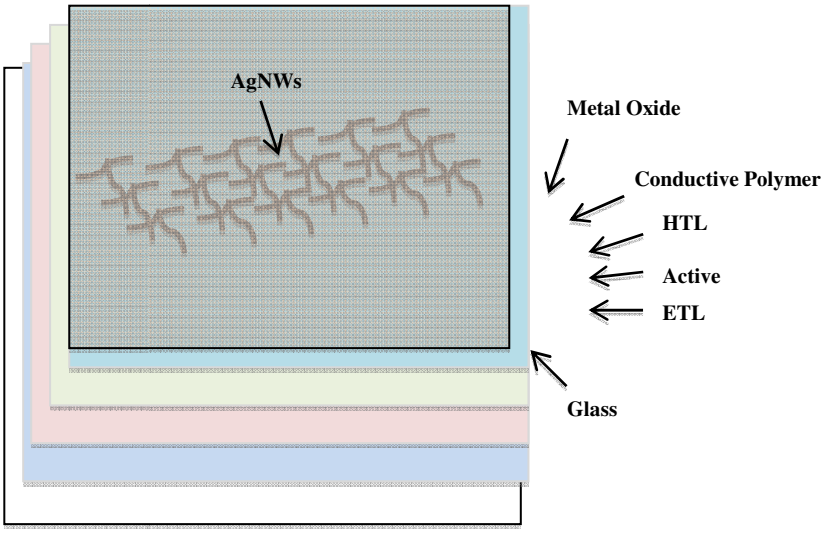


**Figure 9.** Schematic illustration of a double heterostructure OPV cell consisting of a ETL (electron transport layer), active layer, HTL (hole transport layer) and the top contact electrode.

The anode consists of a conductive polymer with submerged AgNWs and spin deposited solution processed metal oxide. It is the principal object of the intended experimental procedure since the top contact electrode determines the overall conductivity and efficiency of the cell. In implementing a composite anode with low sheet resistance and a metal oxide layer, free charge carriers will be able to easily dissociate from an excition in the active layer and collect at their respective electrodes.

On top of the HTL layer, a conductive polymer was deposited by means of spin coating, resulting in a thickness estimated to be 100 nm. Doping concentration of a polar solvent was increased in the polymer by 5%, 10%, and 20%. AgNWs were purchased from from an outside source with length and diameter dimensions of 20 µm and 30 nm, respectively. Spray deposition methods were implemented, while varying three AgNW concentrations

via the addition of spray passes. Increasing the number of low resistance paths that free charge carriers can traverse across has the potential to increase the conductivity of the cell. However, increasing the number of AgNW contacts could increase sheet resistance. A final hole extraction metal oxide layer was spin deposited on top of the AgNWs.

Upon comparing the three doping concentrations in the conductive polymer and the three spray passes of AgNWs, nine samples were measured for sheet resistance (Table I).

**Table I. Sample Matrix for Sheet Resistance Testing**

| Number of Passes | Doping Concentration | | |
|---|---|---|---|
| | 5% | 10% | 20% |
| **Six** | 1 | 2 | 3 |
| **Three** | 4 | 5 | 6 |
| **One** | 7 | 8 | 9 |

### III.II Film Characterization

All sample characterization preparation was performed under a fume hood with the ventilation turned on. Nitrile gloves and safety glasses were utilized when handling samples.

#### III.II. I Sheet Resistance Measurement

The top contact electrode sheet resistance of all nine samples was measured with a four-point collinear probe. A Signatone S-301 four-point probe was utilized with am SP4-50-85 probe tip. This was connected to a HP-6186C DC Current Source and an Agilent 34405A-5 ½ Digital Multimeter (DMM). A range of 1 mA and maximum voltage of 5mV was set on the HP current source. As the probe made contact with the sample surface, current was increased from 0 to 50%, thus using a current of 0.5 mA. Figure 10 displays the four evenly spaced probes measuring the center of a semiconductor material. Current is distributed through the two outer probes while the two inner probes measure the voltage drop.

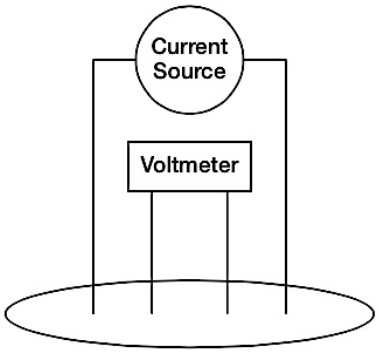


**Figure 10.** Four - Point Collinear Probe Resistance Configuration[11]

After recording the voltage drop (**V),** sheet resistance, $\mathbf{R_s}$, was calculated with Equation 1:

$$\mathbf{R_s(\Omega)} = \frac{\pi}{ln(2)} \times \frac{V(mV)}{i(mA)} \approx \mathbf{4.53} \times \frac{V}{i} \qquad (1)$$

where *i* is the sourced current flow across the surface. Three voltage drop measurements were calculated at the center of each sample and the average sheet resistance was calculated and recorded.

### III. II. II Surface Roughness Characterization

An Asylum MFP-3D Stand Alone Atomic Force Microscope (AFM) was utilized to characterize root mean square (RMS) roughness of the anode with AC (tapping) Mode Imaging in Air. Standard Olympus AC160TS-R3 Silicon probes were implemented in the scanning of each sample. Height change of sample surfaces was detected with a light beam reflecting off the top of the oscillating cantilever and hitting a photo diode sensor (Figure 11). The cantilever is attached to a piezoelectric actuator that converts voltage input into "oscillatory motion that drives the base of the cantilever". [12] As the cantilever scans the surface of the sample, the oscillation amplitude increases and decreases as the cantilever deflects to match the domains of a valley or peak. RMS amplitude ($A_{rms}$) is the standard deviation of the oscillating amplitude that incorporates the cantilever deflection ($Z_i$) and any constant offset ($Z_{const}$) (Equation 2). [12]

$$A_{rms}(V) = \sqrt{\sum_i (Z_{const} - Z_i)^2} \qquad (2)$$

RMS roughness (nm) is then calculated by Asylum software by multiplying the RMS amplitude by the inverse of the optical lever sensitivity, or the amount of cantilever deflection detected by the photo diode.[12]

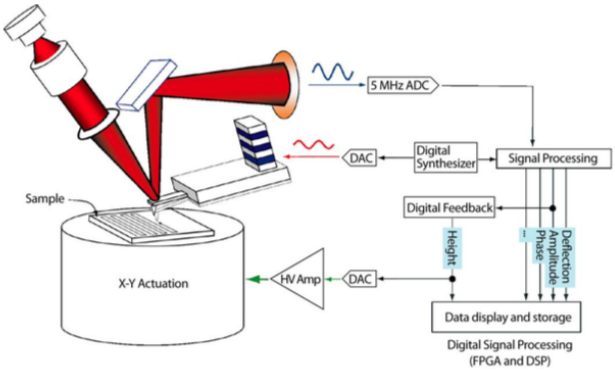


**Figure 11**. Schematic illustration of AC Mode AFM Imaging.[12]

Each sample was mounted (glass substrate side down) on a mica slide with double sided adhesive tape prior to imaging. Six high quality 30µm scans were performed on each sample (Figure 12) with a scan rate of 0.5 Hz and points and lines set to 1024. A -5% target percentage was input into the system and the AutoTune software selected a resonance frequency that provided the greatest free amplitude to match the fundamental oscillation frequency of the cantilever (typically around 354 Hz). Drive amplitude and integral gain were further calibrated once scanning commenced to ensure the phase was in the repulsive region. Recorded drive amplitude values ranged from 20-50 mV, while integral gain values ranged from 30-50. Remaining parameters were left standard to program values (including the set point).

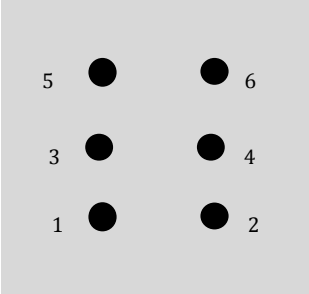


**Figure 12.** Portraying the six scan locations to characterize each sample.

The six Z-sensor RMS roughness values, cumulative average, and standard deviation values were recorded for the 10% doping samples of each AgNW concentration and each doping concentration of the one-pass samples. Each scan was analyzed with Asylum software for topographical points that would significantly alter RMS roughness values. Topographical occurrences such as AgNW agglomeration, large densities of wire-to-wire contact, or accumulated dust particles would produce outlying RMS values.

### III.II.III Nanowire Density Characterization

Samples characterized by the AFM were imaged with a Scanning Electron Microscope (SEM) FEI Quanta 200. The number of AgNW disjoints were quantified by characterizing ten random locations at 20,000 x magnification and a 45-degree angle tilt. Tilting the stage enabled a three-dimensional visual to view topographical discrepancies recorded by AFM characterizations. Samples were prepared by wrapping adhesive conductive copper tape across the bottom glass substrate and 2mm over each edge of the sample (being sure to make contact with top contact electrode). A conductive double-sided adhesive dot was placed in the middle of the copper taping (glass substrate side), as well as the SEM sample stub.

SEM images were attained with the primary beam source set to 1 kV at high vacuum and a 100 Pa pressure. This focused electron beam targeted the surface of the sample, emitting secondary electrons from topographical features. xT Microscopy software translated emitted electrons with the electron detector, thus producing an image. Images

produced at 1 kV may not produce top quality images, however "burning" of the conductive polymer would occur if primary beam voltage were increased further.

## IV. Results and Discussion

### IV. I Sheet Resistance Measurement

Four point probe result averages (Table II) display a significantly higher sheet resistance in the one-pass samples when compared to the three and six pass samples.

**Table II. Sample Sheet Resistance (Ohms/Sq.) Testing**

| Number of Passes | Doping Concentration | | |
|---|---|---|---|
| | 5% | 10% | 20% |
| **One** | 52160.53 | 10655.25 | 5104.48 |
| **Three** | 46.02 | 46.53 | 40.39 |
| **Six** | 21.28 | 23.01 | 18.00 |

Statistical analysis was performed with Minitab software in order to determine if varying AgNW concentration or doping concentration of the conductive polymer produced statistically significant differences in sheet resistance data. Generalizations were made with an interaction plot, after taking the logarithm of based 10 to sheet resistance data. Interaction analysis could not be performed due to a lack of sample replicates. A General Linear Model (GLM) with Tukey comparisons was carried out to determine the statistically significant differences between AgNW concentration and conductive polymer doping (Figure 13).

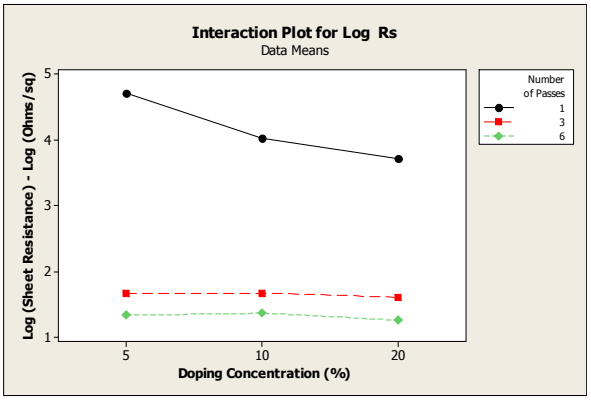


**General Linear Model: Log Rs versus Passes, Doping**

```
Factor   Type    Levels  Values
Passes   fixed        3  1, 3, 6
Doping   fixed        3  5, 10, 20

Analysis of Variance for LogMean Rs, using Adjusted SS for Tests

Source   DF   Seq SS   Adj SS  Adj MS      F      P
Passes    2  14.4278  14.4278  7.2139  89.35  0.000
Doping    2   0.2176   0.2176  0.1088   1.35  0.357
Error     4   0.3230   0.3230  0.0807
Total     8  14.9683

S = 0.284146   R-Sq = 97.84%   R-Sq(adj) = 95.68%

Grouping Information Using Tukey Method and 95.0% Confidence

Passes   N   Mean  Grouping
1        3  4.151   A
3        3  1.646    B
6        3  1.315    B

Means that do not share a letter are significantly different.
```

**Figure 13.** Left) Interaction plot displaying the large sheet resistance difference of one pass compared to three and six. Doping concentration highly affected sheet resistance in one pass. Right) Minitab output displaying the statistically significant difference between one pass and three and six.

From observing the interaction plot, it is clear that sheet resistance is dramatically higher with one pass of AgNWs when compared to three and six. GLM analysis supports this conclusion, as there are grouping differences between the one-pass and three and six passes and a P value close to zero. Further analysis of the three and six pass samples were performed since there were no grouping differences between them (Figure 14). Additionally, there were no grouping differences between doping concentrations when compared with the three AgNW concentrations. However, it is clear from Figure 12 interaction plot that sheet resistance in one pass decreases with increasing doping concentration.

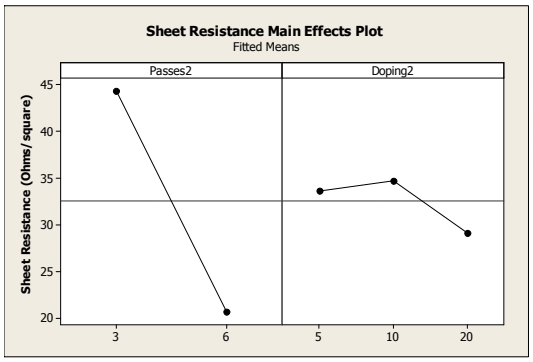


```
Grouping Information Using Tukey Method and 95.0% Confidence

Passes2  N   Mean  Grouping
3        3  44.31    A
6        3  20.77    B

Means that do not share a letter are significantly different.

Grouping Information Using Tukey Method and 95.0% Confidence

Doping2  N   Mean  Grouping
10       2  34.77   A
 5       2  33.65   A B
20       2  29.20     B

Means that do not share a letter are significantly different.
```

**Figure 14.** Left) Main effects plot illustrating the factor of two difference between AgNW density and the average decrease in sheet resistance with increase doping. Right) Minitab output displaying the statistically significant difference between 5% doping concentration and 20%.

The main effects plot of raw mean sheet resistance data displays a factor of two decrease in sheet resistance when increasing AgNW concentration from three to six passes. GLM analysis of three and six passes portrayed grouping differences between AgNW densities with a P-value close to zero. Failure to display this statistical difference in the previous interaction plot may have been attributed to Minitab attempting to average the one-pass sheet resistance results that were orders of magnitude greater, thus unable to accurately analyze differences within the three and six passes. Grouping differences in polymer doping concentration were also observed between 10% and 20% with a P-value of 0.038. However, only a 5.57-Ω/sq. difference resulted from increasing doping concentration when compared to the 23.54-Ω/sq. difference from increasing AgNW concentration.

We have articulated two resistance models in an attempt to explain trends in sheet resistance data attributed to low AgNW concentrations (one-pass) and high AgNW concentration (three and six passes). Both models were based on a simple resistance model that assumes current or free charge carriers run through ideally straight AgNWs on a uniformly flat surface (Figure 15). However, due to the substantial amount of wire-to-

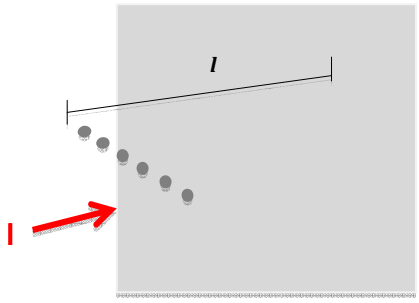


**Figure 15**. The ideal model for the conduction of free charge carriers through AgNWs.

wire contact (illustrated in section IV.II and IV.III), disjointed regions between AgNWs, an increased roughness due to increased polymer doping and AgNW concentration, etc., a fudge factor □ was incorporated into equation 3:

$$R = \vartheta\left(\rho\frac{l}{A}\right) = \vartheta\left(\frac{\rho}{t}\right)\left(\frac{l}{w}\right) \tag{3}$$

where □ represents the resistivity of the bulk material, □ represents the length of the sample, □ represents the area of the surface being measured, $t$ represents the thickness, and $w$ represents the width.

Single pass AgNW samples may be represented as resistors in series that follow equation 4:

$$R_{eq} = R_{CP} + R_{AgNW} \tag{4}$$

where $R_{CP}$ is the resistance of the conductive polymer and $R_{AgNW}$ is the resistance associated with the AgNWs. Sheet resistance values are orders of magnitudes higher than high concentration AgNW samples due to the free charge carriers traversing across the chains of the conductive polymer after reaching disjointed regions of AgNWs

(Figure 16). This phenomenon is further illustrated with SEM characterizations in section IV.III.

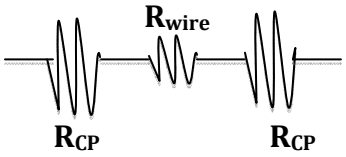


**Figure 16.** Schematic diagram supporting the resistors in series model.

Because free charge carriers are forced to depend on the polymer for conduction, we can assume that the decrease in sheet resistance is due to the increase in doping concentration of the polymer. We can make this assumption based on how the polymer's resistance of 52k-Ω/sq. makes the 20-Ω/sq. resistance of the AgNWs almost negligible in our resistors in series model.

Computations in order to determine an estimated resistance value due to the conductive polymer have been performed. Equations 5 and 6 display the assumption that the measured resistance, $R_{eq}$, of the one pass samples is relatively equal to the resistance of the polymer.

$$R_{eq} \approx R_{CP} \tag{5}$$

$$R_{eq} = \cancelto{0}{R_{s-AgNW}} \cdot t_{AgNW} + R_{s-CP} \cdot t_{CP}$$

$$R_{eq} \approx R_{s-CP} \cdot t_{CP} \tag{6}$$

$R_{S\text{-}CP}$ represents the sheet resistance due to the conductive polymer and $t_{CP}$ represents the thickness of the conductive polymer. In calculating the ratio of the estimated thickness of the conductive polymer layer to the AgNW diameter, we obtain a value of 3.33. We can then estimate $R_{S\text{-}CP}$ by imputing the thickness ratio multiplied by the diameter of the AgNW, $t_{AgNW}$, into equation 7.

$$R_{s-CP} \approx \frac{R_{eq}}{3.33 \cdot t_{AgNW}} \tag{7}$$

In plotting the measured one-pass sheet resistance values to the calculated $R_{S\text{-}CP}$ values (Figure 17), a slope of one is produced. This supports our resistors in series model and

our assumption that the measured high sheet resistance values are a result of free charge carriers depending on the polymer for conductance.

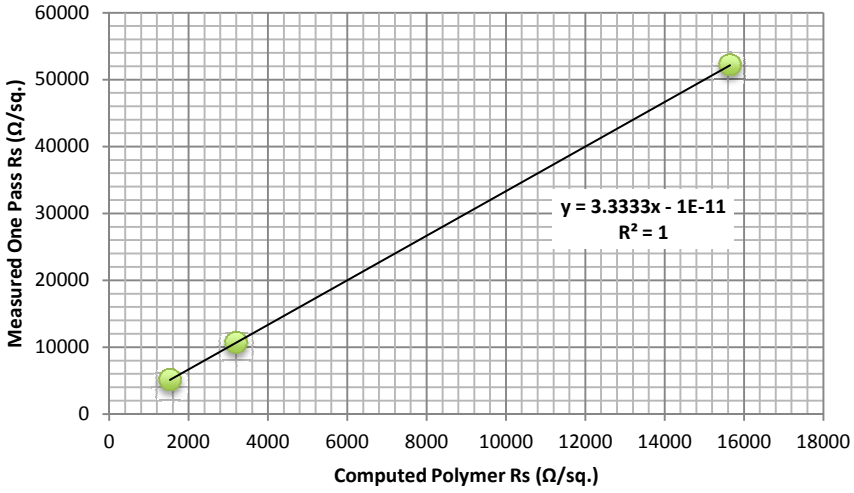


**Figure 17.** Displaying the comparison between the computed polymer sheet resistance and the one pass measured sheet resistance values.

High AgNW concentrations may be best represented by resistors in parallel, as free charge carriers can depend on AgNWs for conduction, but also utilize the increased conductivity as doping concentration in the polymer is increased (equation 8).

(8)

As there is a greater number of AgNWs for free charge carriers to conduct across, there is a lower probability that the conductive polymer will be utilized for conduction. AgNWs lie on top or are partially submerged in the conductive polymer, creating a circuit as displayed in Figure 16.

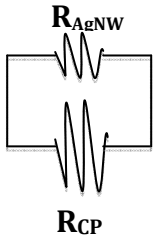


**Figure 16.** Schematic diagram displaying two conducting paths that free charge carriers can take.

In using the proposed resistors in parallel model for the three and six pass samples, we can estimate the resulting sheet resistance due to the AgNWs, $R_{S\text{-}AgNW}$. Calculations are performed by imputing the calculated $R_{S\text{-}CP}$ values for $R_{CP}$. and imputing our measured sheet resistance values for $R_{eq}$. We can then plot $R_{S\text{-}AgNW}$ compared to the expected theoretical AgNW sheet resistance values found in literature (Figure 17). The red trendline represents ideal values that we would expect to measure: 20-Ω/sq. and 40-Ω/sq. for the six and three pass samples, respectively. Theoretical AgNW sheet resistance values for the three pass samples are expected to be double those of the six pass samples. As the concentration of AgNWs that span the width of the electrode surface increase by a factor of two with six pass samples, computed AgNW sheet resistance values will be closer to the theoretical 20-Ω/sq. bulk sheet resistance of AgNWs. This factor of two difference was also seen in the main effects plot of Figure 14. Lower sheet resistance values are a result of higher AgNW concentrations as free charge carriers can depend on AgNWs for conduction.

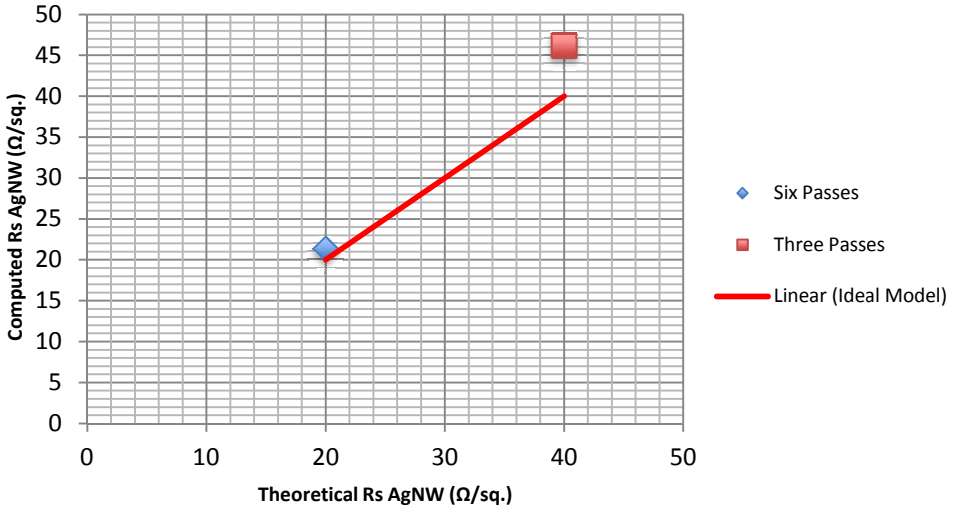


**Figure 17.** Illustrating how computed AgNW sheet resisance is almost equal to expected theoretical AgNW sheet resistance values.

Computed $R_{S\text{-}AgNW}$ values were found to be 12.38 % higher than theoretical values in the three pass samples and 4.51 % higher in the six pass samples. A greater percent difference in the three pass samples can be attributed to a higher fudge factor (Equation 3), where there are still some regions of disjoint between AgNWs. This is will be displayed in SEM characterizations in section IV.III.

## IV. II. Surface Roughness Characterization

As expected, the average RMS roughness increased as the number of AgNW spray passes increased (Table III).

**Table III. Increase in RMS with Increase AgNW Concentration**

| Number of Passes | Average RMS (nm) |
|---|---|
| **One** | 26.70 |
| **Three** | 40.11 |
| **Six** | 66.20 |

A substantial amount of variance was found throughout all characterized samples (Figure 18). Variance in data is attributed to sporadic height differences as a result of AgNW

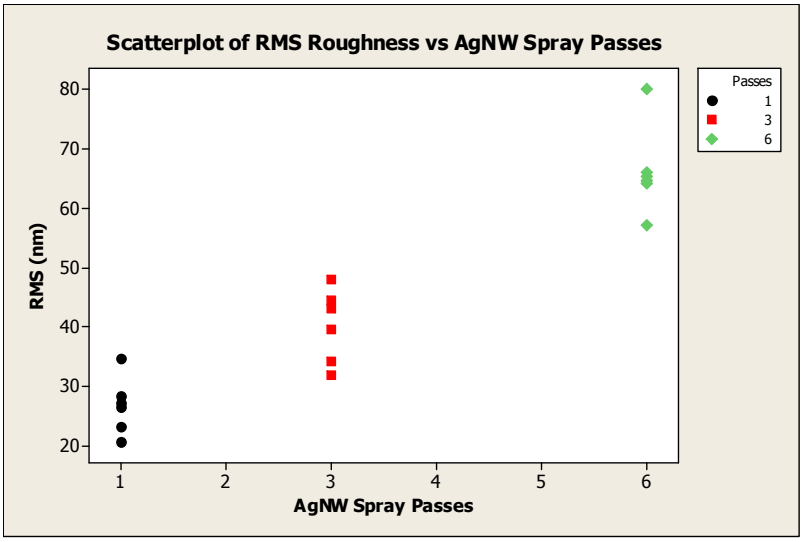


**Figure 18.** Statistically significant differences in RMS roughness due to increasing AgNW spray passes. Variances within data is displayed

agglomeration, what is thought to be AgNW fragments and nanoparticles, curved and ring-like AgNW orientations and dust particles. The potential of an increase in roughness due to the metal oxide was disregarded since all samples were given identical metal oxide spin deposition processing. AFM images of increasing RMS roughness due to increasing AgNW concentration are portrayed in Figure 19.

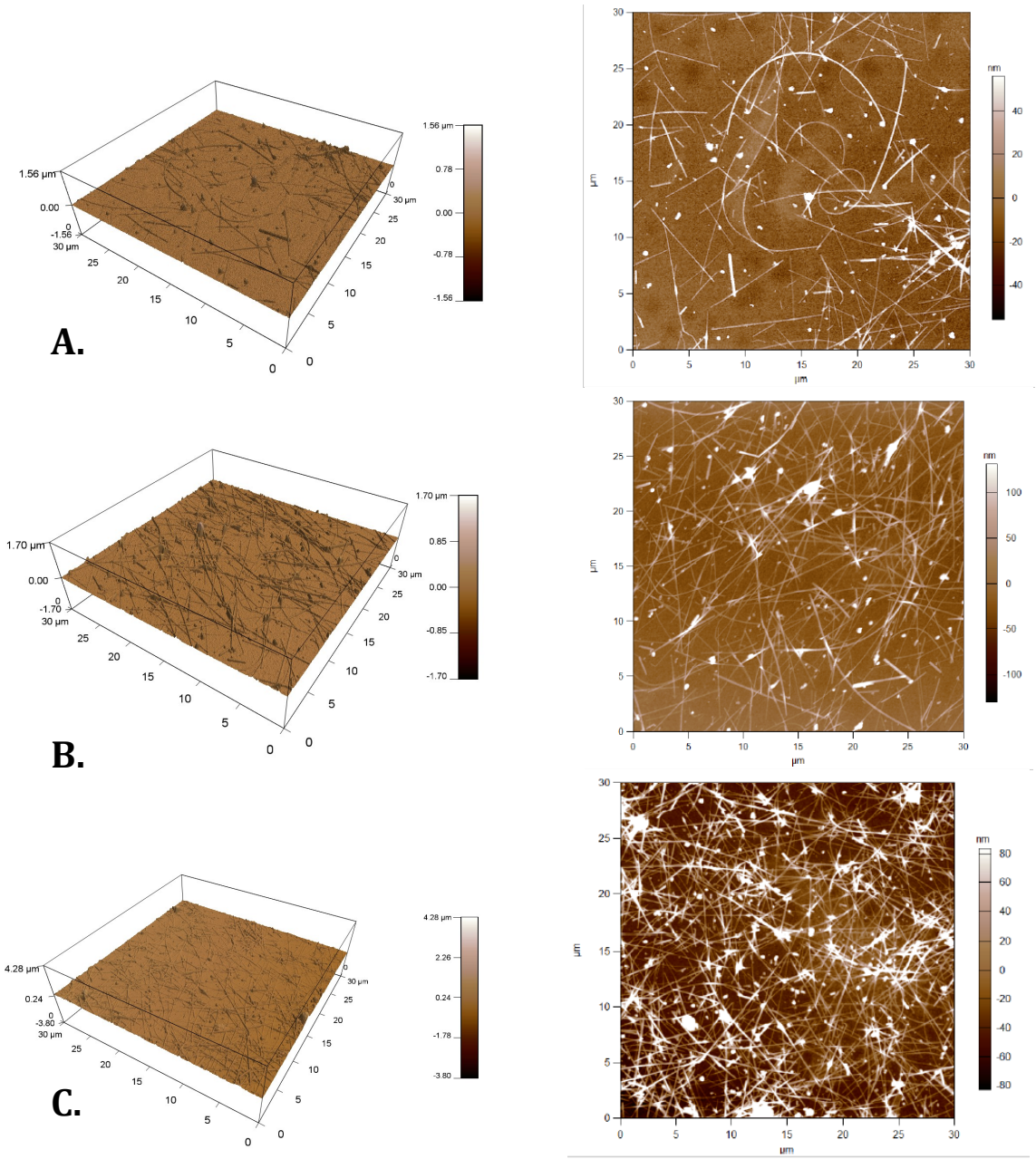


**Figure 19.** Three-dimension and corresponding flat AFM images of A) one pass B) three pass and C) six pass.

From the roughness scale accompanying AFM characterizations in Figure 19, six and three pass samples display areas of AgNW agglomeration much more than the one-pass. It is valid to state that as AgNW concentration increases, AgNW agglomeration increases as well. Hypothetically, agglomeration would pose as a detriment to sheet resistance due

to increased wire-to-wire contact, which would produce more areas of wire-to-wire contact resistance. We have seen that sheet resistance values significantly decrease with increasing AgNW concentration. However, because AgNW agglomeration was present (Figure 20), measured RMS roughness values could not accurately estimate average distances between AgNWs in contact or the distance between AgNWs and the conductive polymer. If these average distances were known, more accurate sheet resistance results and conclusions could be drawn.

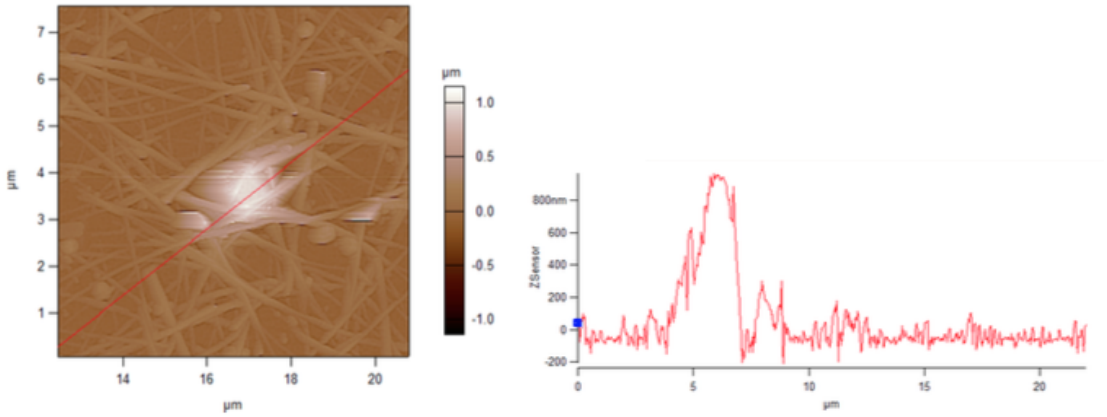


**Figure 20.** Zoomed in display (left) on AgNW agglomeration peak with corresponding height graph (right).

In addition to AgNW agglomeration, curvatures of AgNWs into circular rings were found across all samples. In cases where tightly formed rings were lying, adjacent AgNWs and those lying on top of rings increased RMS roughness values (Figure 21). If AgNWs were

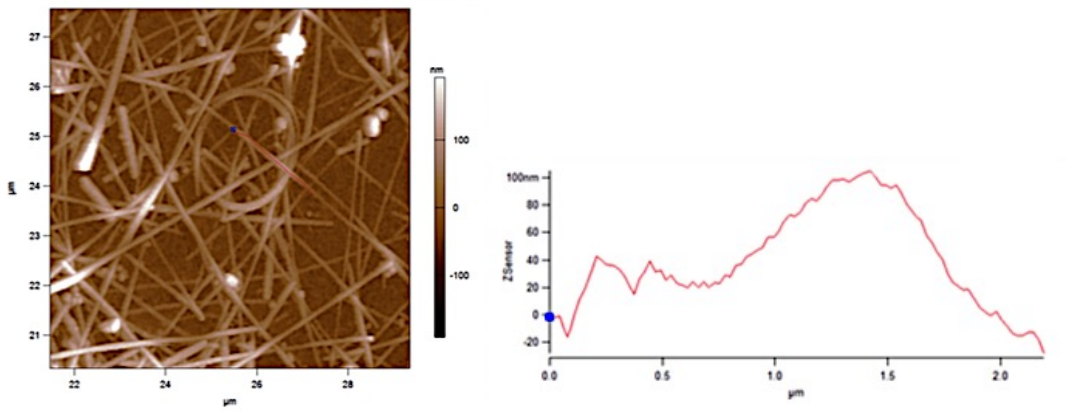

**Figure 21.** Expanded AFM view of tight circular rings in with corresponding height graph.

to follow the ideal sheet resistance model, RMS values would resemble the diameter of the AgNWs (30nm). With AgNWs lying across ring-like wire formations, Figure 21 displays a height increase to 100nm.

It is unclear exactly why AgNWs take circular or curved orientations instead of lying straight. In order for a wire to curve, one side of the wire would need to be in tension while the other in compression. Drying of the spray deposited AgNWs occur almost instantly in ambient air, which would factor out non-uniform drying as a potential cause. Throughout the surface, it was also clear that nanoparticles were randomly dispersed across the surface. Some of these particles appear to be under AgNWs, which will be displayed in SEM characterizations. This alludes to the possibility of those particles being silver nanoparticles (AgNP) that were present in the solution prior to spray deposition. If AgNWs were growing in solution with the polypol method, there is a possibility that silver atoms did not attach to the faces of the decahedra surface of the Ag seeds, and thus did not form AgNWs.[4] Additionally, AgNWs may have warped into ring or bent orientations in the solution prior to spray deposition, but the exact cause is unknown. Figure 22 displays what is thought to be a micro sized dust particle that landed on the electrode surface post AgNW spray deposition when compared to what is thought to be an AgNP.

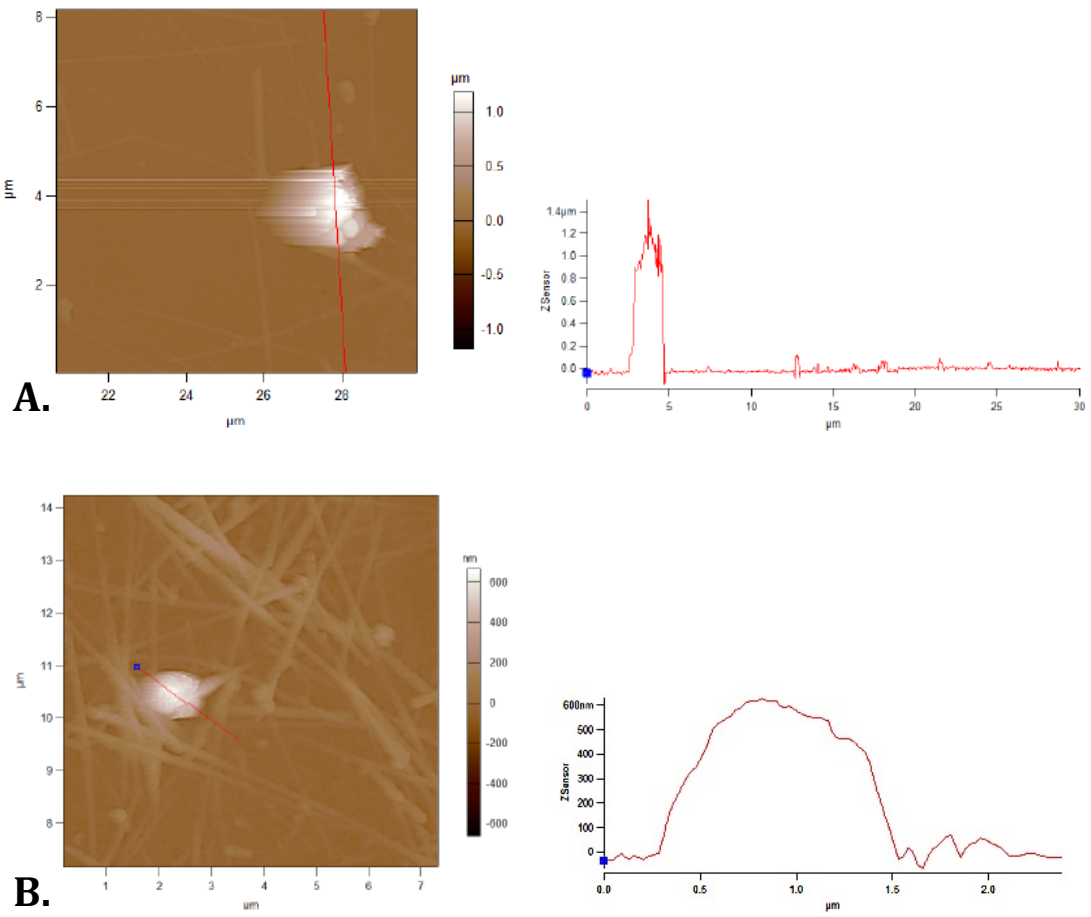


**Figure 22.** Zoomed in display (left) of AgNW agglomeration peak with corresponding height graph (right). A) A 1.4 µm sized dust particle that has landed on the electrode surface. B) A 600 nm sized AgNP that was deposited during the spray deposition of AgNWs.

As potential AgNPs were found in further examining Figure 19, it was also clear that AgNWs were not of uniform length. Eight curved and eight straight AgNW lengths were measured with AFM analysis software on each one-pass sample (Figure 23). Measurements were performed on one-pass samples due to less wire-to-wire interaction. Results of AgNW measurements displayed a statistically significant length difference due to AgNW orientation. Wires in a curved orientation were on average 15.4 µm compared to a mean length of 11.3 µm for straight wires (Figure 24). Comparing these lengths to the manufacturers dimensions of 30µm results in a length difference of 14.6 µm for curved wires and 18.7 µm for straight wires. No statistically significant length differences due to increased doping were obtained.

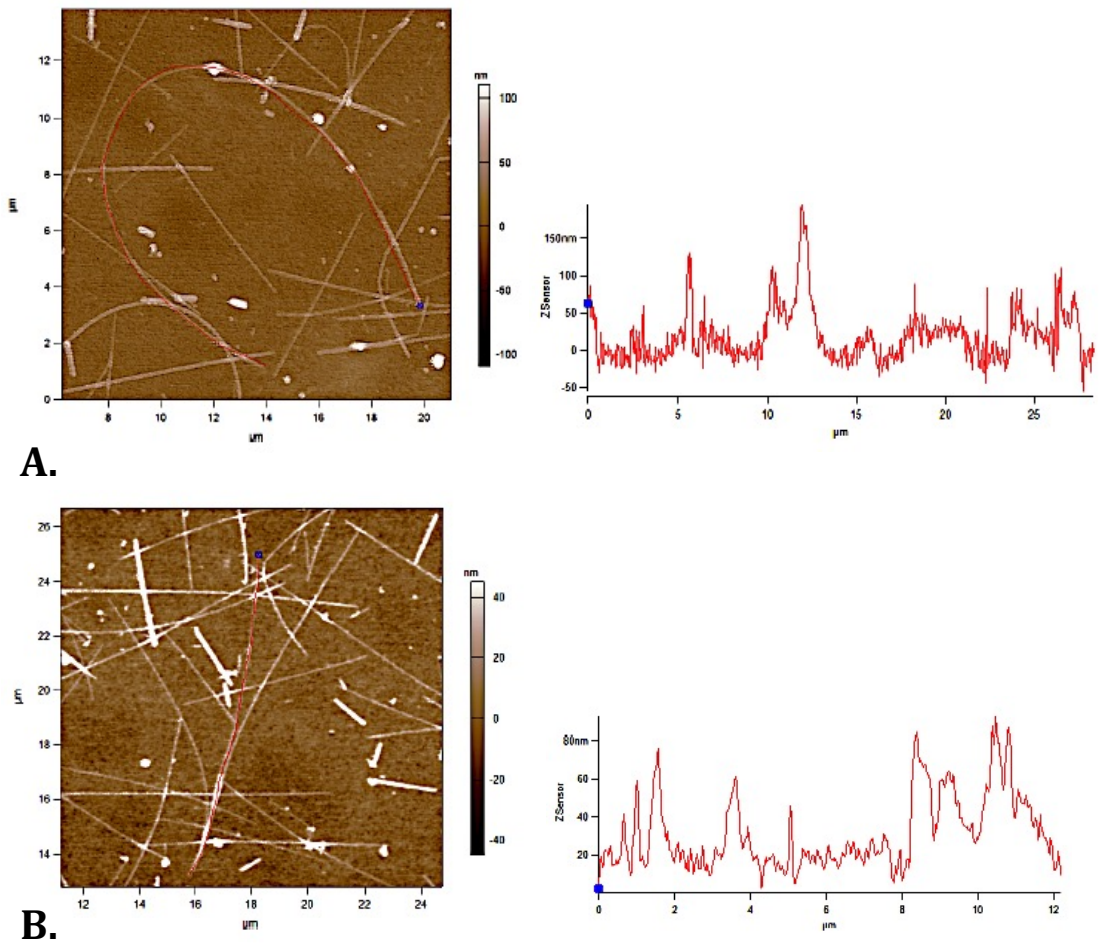


**Figure 23.** Length trace with corresponding graph giving trace measurement of A) curved and B) straight AgNW.

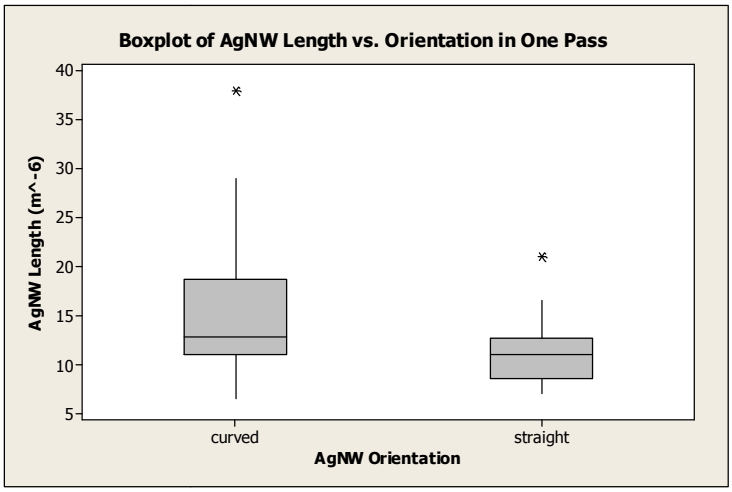


**Figure 24**. Difference in AgNW lengths due to the orientation that wires were deposited with.

Differences in lengths due to the curved or straight formation of the wire reveals the possibility of wires fracturing upon impact during spray deposition. If making the assumption that 30 µm long curved wires were in the solution prior to deposition, wires may have fractured at the point of curvature upon impact during deposition. This would result in wire fragments of varying lengths. Wires that maintained curved orientation would thus be expected to be longer than straight wire fragments. However, it is a possibility that wires merely did not grow up to 30µm lengths in solution. This may be a valid assumption if AgNPs are present.

Shorter AgNWs are detrimental to sheet resistance results as more regions of disjoints appear in low AgNW concentrations, and a greater AgNW concentration are needed in order for free charge carriers to have sufficient conducting paths. AgNWs with smaller aspect ratios require more contact points and thus have more points of contact resistance. Additionally, more AgNWs covering the surface of the electrode would be detrimental to optical properties, such as transparency, and would lower the overall efficiency of the cell.

RMS roughness values of one-pass samples were obtained as studies show conductive polymer roughness increases with increasing doping concentration (Table IV).

**Table IV. Increase in RMS with Polymer Doping Concentration**

| Doping Concentration (%) | Average RMS (nm) |
|---|---|
| **5** | 24.93 |
| **10** | 25.48 |
| **20** | 29.69 |

Although RMS values portrayed a slight increase in roughness, results were not statistically significant. This is attributed to the large amount of variance across one-pass sample surfaces (Figure 25).

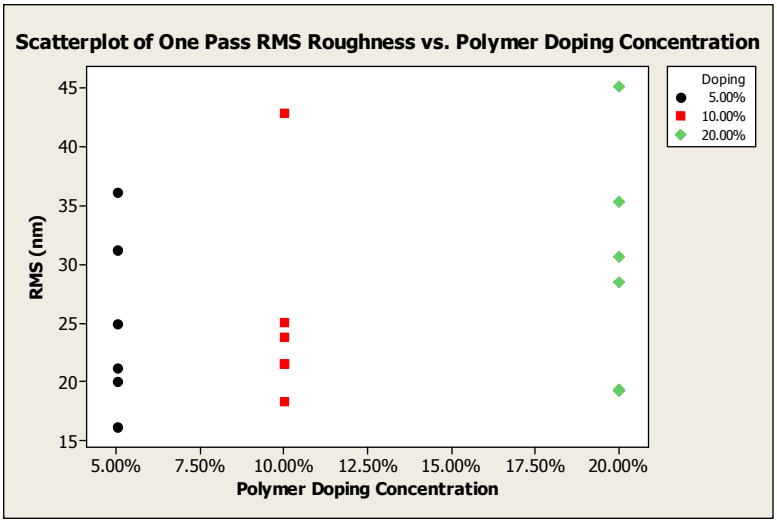


**Figure 25.** Variance in roughness values in one-pass samples producing statistically insignificance RMS values.

Only few outlying RMS roughness values appear to cause the slight increase in roughness with increased doping concentration. In order to accurately decipher roughness differences, samples without AgNWs should be characterized.

### IV. III Nanowire Density Characterization

At 20,000x magnification and a working distance of 6.5 mm, 2.8 µm x 3.2 µm sections of the electrode surface were characterized on the SEM. The number of disjointed regions between AgNWs decreased with increasing AgNW concentration (Figure 26).

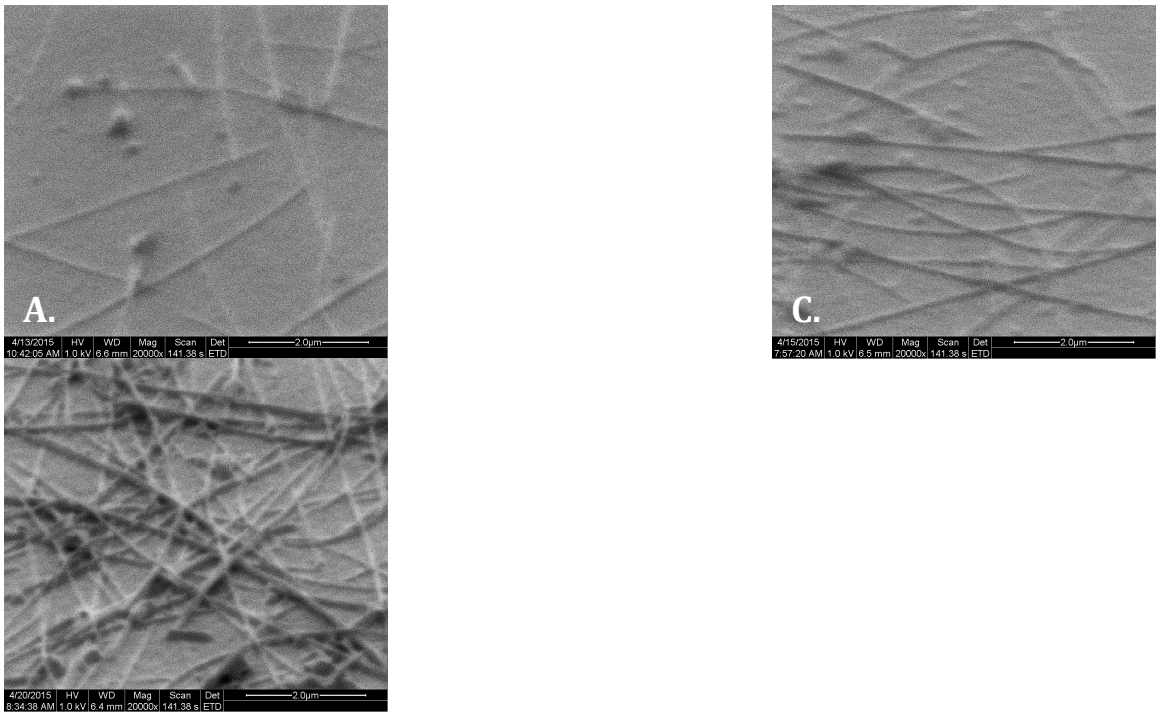


**Figure 26.** Comparing number of AgNW end points of one pass samples. A) Sample 10 B) Sample 11 and C) Sample 12

Disjointed regions across the ten characterized regions of each sample were quantified to approximately two regions per section in one pass, one region in three passes, and zero in the six pass samples. Regions of disjoint in one-pass samples are illustrated in Figure 27.

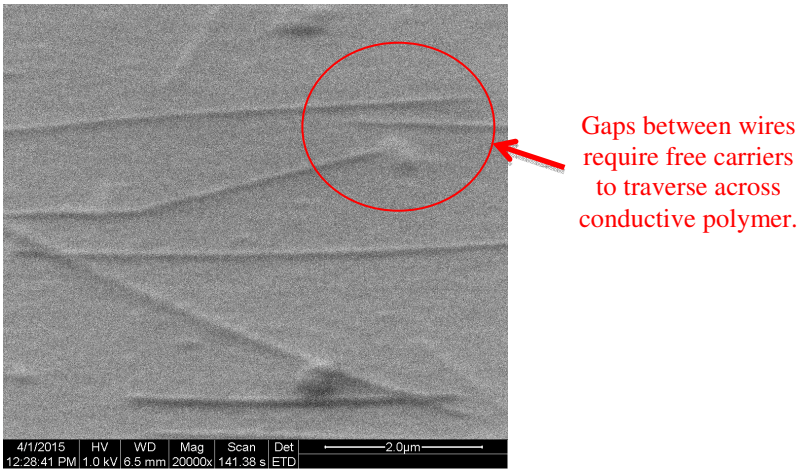

**Figure 27.** Two regions of disjointed displayed in red circle.

In referring back to the one-pass resistors in series model (Section IV.I), this image provides a visual representation of the high resistance path a free charge carrier would traverse across. Agglomeration in three and six pass samples were imaged to further portray wire-to-wire interaction (Figure 28). SEM characterizations of both instances were incorporated into the resistance model fudge factor of Equation 3. AgNWs with high aspect ratios are able to morph over each other, as displayed in the cluster of

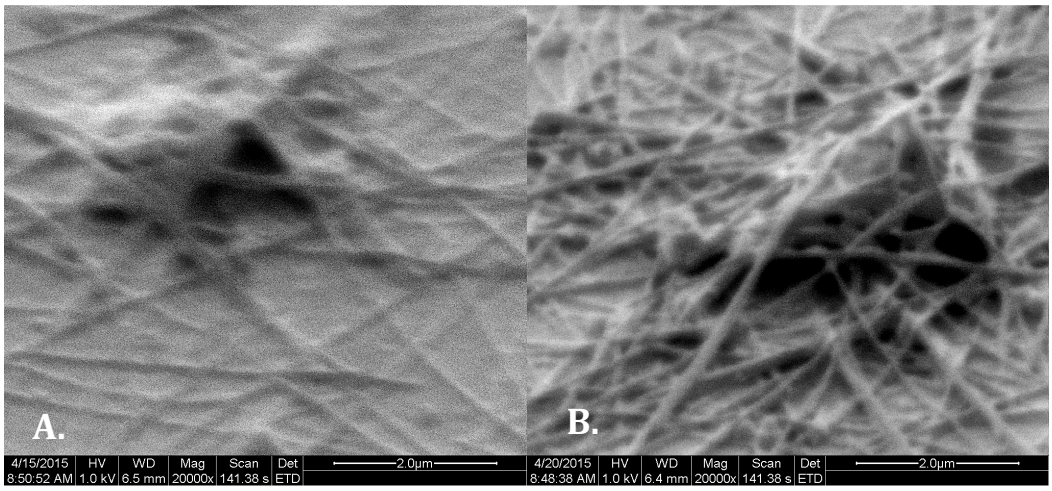


**Figure 28.** Comparing AgNW agglomeration between A) three pass and B) six pass samples.

AgNWs, which may counteract major sheet resistance increases as free charge carriers travel the most direct path of least resistance.

As AFM characterizations found short wire lengths and potential AgNPs, SEM characterizations displayed wire interaction with AgNPs and wire fragments (Figure 29).

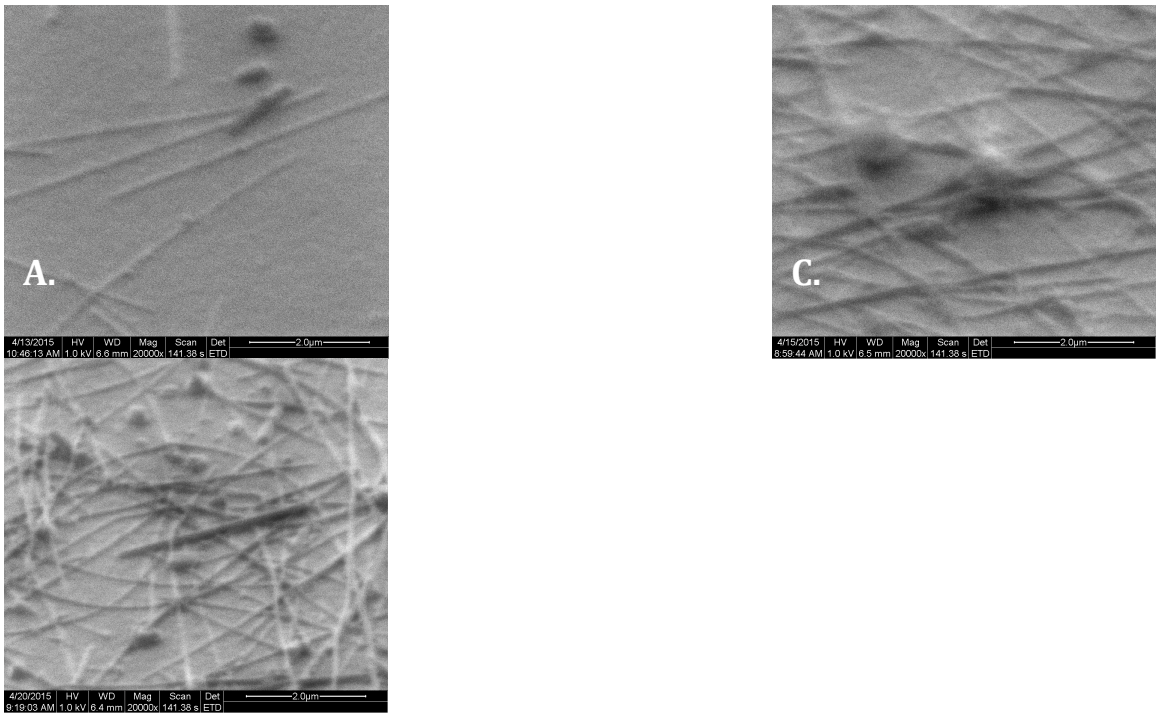


**Figure 29.** Wire fragments and AgNPs within A) one pass B) three pass and C) six pass samples.

Figure 29 A) displayed a wire fragment causing unnecessary wire-to-wire contact resistance, as well as AgNPs. AgNPs may contribute to increasing contact resistance and may also be detrimental to optical properties. Figure 29 B) displays the potential AgNPs with AgNWs overlapping. With AgNWs overlapping, we can imply that particles were from the AgNW dispersion prior to deposition. Additionally, from the six-pass image, there appears to be a larger concentration of AgNPs that could potentially cause more contact resistance. Further analysis of AgNPS and their effects should be researched.

## V. Conclusion:

Sheet resistance measurements of the top contact electrode layer resulted in a series resistance model for a one-pass AgNW concentration, and a parallel resistance model for three and six passes. These models explained how higher AgNW concentrations with more conductive paths for free charge carriers produce more efficient and lower sheet resistant electrodes. However, AgNWs should be inspected for consistent dimensions prior to deposition, as AFM results portrayed wires to be on average 18.7µm for a curved orientation and 11.3 µm for straight orientations. SEM results illustrated the reduction of two disjointed AgNW regions in one pass samples, to zero in six pass samples. An ideal top contact electrode would contain a lower concentration of AgNWs with consistent high aspect ratios. This would produce a low sheet resistance and high transparency electrodes.

Further research of increased roughness due to increased doping concentration should be characterized with the AFM without AgNWs. Additionally, characterizations should be performed on samples without the metal oxide, and some with only AgNWs. Comparing results of samples without metal oxide will enable more conclusions on the effect of the metal oxide to the sheet resistance of the cell. Analyzing samples with only AgNWs and conductive polymer without any doping concentration will produce more accurate sheet resistance results and models.

## VI. References:


1. Lai, Tzung-Han, Sai-Wing Tsang, Jesse R. Manders, Song Chen, and Franky So. "Properties of Interlayer for Organic Photovoltaics." Materials Today 16.11 (2013): 424-32. Web.
2. David Cohen. 2007. Earth's Natural Wealth. New Scientist. pg. 32-41
3. Araki, T. et al., 2013. Low haze transparent electrodes and highly conducting air-dried films with ultra-long silver nanowires synthesized by one-step polyol method. Nano Research, 7(2), pp.236–245.
4. Ye, S. et al., 2014. Metal Nanowire Networks: The Next Generation of Transparent Conductors. Advanced Materials, 26(39), pp.6670–6687.
5. Gaynor, W. et al., 2011. Smooth Nanowire/Polymer Composite Transparent Electrodes. Advanced Materials, 23(26), pp.2905–2910.
6. R. H. Friend, R. W. Gymer, A. B. Holmes, J. H. Burroughes, R. N. Marks, C. Taliani, D. D. C. Bradley, D. A. Dos Santos, J. L. Bredas, M. Logdlund & W. R. Salaneck, "Electroluminescence in conjugated polymers," Nature, 397, 1999 p. 121-128.
7. Heraeus. Conductive Polymers. Issue brief. Heraeus Clevios GmbH, n.d. Web. Dec. 2014.
8. Keawprajak, Anusit, Wantana Koetniyom, Phimwipha Piyakulawat, Kanpitcha Jiramitmongkon, Sirapat Pratontep, and Udom Asawapirom. "Effects of Tetramethylene Sulfone Solvent Additives on Conductivity of PEDOT:PSS Film and Performance of Polymer Photovoltaic Cells."Organic Electronics 14.1 (2013): 402-10. Elsevier. Web.
9. Ouyang, Jianyong. "“Secondary Doping” Methods to Significantly Enhance the Conductivity of PEDOT:PSS for Its Application as Transparent Electrode of Optoelectronic Devices." Displays 34.5 (2013): 423-36. Web.
10. Hancox, I., P. Sullivan, K.v. Chauhan, N. Beaumont, L.a. Rochford, R.a. Hatton, and T.s. Jones. "The Effect of a MoOx Hole-extracting Layer on the Performance of Organic Photovoltaic Cells Based on Small Molecule Planar Heterojunctions." Organic Electronics 11.12 (2010): 2019-025. Web.

**11.** Keithley, ed. "Four-Probe Resistivity and Hall Voltage Measurements with the Model 4200-SCS." Number 2475 (2011): n. pag. Www.keithley.com. Web. Feb. 2015.
**12.** Asylum Research. Installation and Operation Manual. N.d. MS Version 04_08, MFP-3D Manual. Cal Poly - San Luis Obispo, n.p